



Understanding the characteristics, enhanced optical and photoelectrochemical performance of copper-loaded titania nanotubes synthesized via successive ionic layer adsorption reaction

Nur Farah Atikah Harun¹ · Yusairie Mohd¹ · Ying Pei Lim² · Chun-Yang Yin³ · Ying-Chin Lim¹ 

Received: 4 April 2018 / Accepted: 22 June 2018 / Published online: 26 June 2018
© Springer Science+Business Media, LLC, part of Springer Nature 2018

Abstract

The physico-chemical, optical and photoelectrochemical (PEC) characteristics of copper sensitized titania nanotubes (CuTNT) nanocomposites are still not well understood despite numerous conducted studies. In the present study, copper sensitized titania nanotubes (CuTNT) were prepared using customized Successive Ionic Layer Adsorption Reaction (SILAR) method. The foremost aim is to investigate the aforesaid characteristics and consolidate the results to propose mechanisms to elucidate CuTNT's enhanced optical and PEC performance. Such mechanisms are of particular interest because a better understanding of them would essentially translate to advances in improved CuTNT production and use, especially in regard to PEC applications. We, therefore, attempt to shed more light on its characteristics by employing electron microscopies, X-ray powder diffraction and X-ray photoelectron spectroscopy techniques. Well-ordered crystalline TNT was successfully obtained via anodization in the mixture of ethylene glycol and water mixed with NH_4F . CuTNTs were prepared at various concentrations, SILAR cycles and immersion times. CuTNT/20 min of fixed 20 mM and 3 SILAR cycles showed enhanced photoconversion efficiency of almost 2.7 times higher compared to pure TNT due to electron-trap center effect introduced by Cu, reduced band gap energy from 3.26 eV of pure TNT to 2.75 eV, enhanced visible light reactivity and balanced distribution within TNT.

1 Introduction

Since the discovery of water splitting using TiO_2 by Fujishima in 1972, TiO_2 is widely utilized in photocatalytic applications due to its suitable band gap with band edges that pass water redox potentials [1]. Such applications require the highly reactive surface of TiO_2 but producing TiO_2 nanoparticles is unfavourable due to the possibility of recombination of electron–hole pairs [1]. The high recombination rate between electron–hole pairs also contributes towards its low electrical conductivity. Additionally, its wide

band gap limits its utilization to only UV light spectrum [2] and not visible light spectrum.

Hence, various TiO_2 modifications were investigated to circumvent the aforesaid drawbacks, which include surface modifications such as fabrication of TiO_2 as nanotubes (TNT) to increase the active surface areas; as well as deposition of other narrow band gap materials onto TiO_2 to improve TiO_2 absorption of visible light and reduce the recombination rate. Studies on the depositions of various dopants have been extensively reported including metals, noble metals, metal oxides, metal chalcogenides and non-metals. Performance enhancements of various process parameters due to such depositions are summarized in Table 1.

However, the option of environmental friendly and low-cost materials should be taken into account if green and low-cost fabrication is desired. For example, chromium is less environmental friendly and toxic whereas noble metals such as platinum and silver are expensive and therefore these materials are less suitable to be chosen as a dopant.

Copper is one of the most suitable metals that can overcome these limitations since it has a narrow band gap.

✉ Ying-Chin Lim
limyi613@salam.uitm.edu.my

¹ Faculty of Applied Sciences, School of Chemistry and Environment, Universiti Teknologi MARA, 40450 Shah Alam, Selangor, Malaysia

² Faculty of Chemical Engineering, Universiti Teknologi MARA, 40450 Shah Alam, Selangor, Malaysia

³ Newcastle University in Singapore, 537 Clementi Road #06-01, SIT Building @ Ngee Ann Polytechnic, Singapore 599493, Singapore

Table 1 Summary of performance enhancement resulted from the deposition of various types of dopants into titania nanotubes

Dopant	Dopant type	Performance enhancement
Cu	Metal	Visible light reactivity and photoresponse [3]
Cr	Metal	Visible light reactivity and hydrogen generation [4]
Ag	Noble metal	Visible light reactivity and photodegradation of phenol [5]
Pt	Noble metal	Photo-oxidation of ammonia [6]
ZnO	Metal oxide	Visible light reactivity and hydrogen generation [7]
WO ₃	Metal oxide	Visible light reactivity and photoconversion efficiency [8]
PbO, WO ₃	Metal oxide	Visible light reactivity, photodegradation of methylene blue [9]
CdSe	Metal chalcogenide	Visible light reactivity and photoresponse [10]
CdS	Metal chalcogenide	Visible light reactivity and photodegradation of dyes [11]
S	Non-metal	Visible light reactivity and hydrogen generation [12]
C	Non-metal	Photoconversion efficiency and hydrogen generation [13]

Other advantages such as high availability, low cost, environmentally friendly characteristic [14], good conductivity and durability [15] render copper a promising dopant. By tuning the morphology of Cu such as varying their shapes and sizes, the properties can be altered to suit specific applications [15]. Studies on the deposition of various Cu species onto TiO₂ are quite extensive and they include the deposition of CuO onto TiO₂ [16], CuO [9], Cu [3], Cu₂O [6, 8, 13], Cu(OH)₂ [17] or even mixtures of Cu species such as CuO/Cu(OH)₂ [18], and Cu (II) ions [19] into TNT. The deposition involves various methods such as Chemical Bath Deposition (CBD), electrochemical deposition, photochemical deposition, and the Successive Ionic Layer Adsorption Reaction (SILAR) method.

SILAR method is widely known as a simple immersion method for deposition of either thin films [17–22] or nanoparticles. The deposition of nanoparticles onto TNT conducted via this method has also been reported [3, 11, 23, 24]. SILAR requires shorter immersion time [25] with simpler chemical preparation and yet it is able to synthesize a more uniformed dispersion of nanoparticles [3] compared to other immersion methods such as the CBD technique and can be considered as environmental friendly. By using this method of deposition, we postulate that Cu loading process could be simplified if a chemical reduction process was incorporated into the SILAR process, which could pave the way for a more cost-effective variation of the SILAR process. So far, there is no identified report that elucidates light illumination mechanisms associated with enhanced optical and photoelectrochemical performance of SILAR-synthesized CuTNTs. As such, this gap of knowledge consequently inspires us to conduct the present study. The objectives of this study include synthesis of CuTNTs via chemical reduction combined SILAR method and characterization of the morphology, elemental composition, chemical composition, band gap energy as well as the determination of the photoconversion efficiency of the resulting CuTNTs.

2 Materials and method

Ti foil substrates (1 × 2 cm²) were cleaned by using an ultrasonic bath. This was followed by an anodization process to convert the Ti pieces into TNT. They were then calcined in 500 °C to induce the crystallinity of the as-anodized TNT. The anodization process was performed as per our previous reported study [26]. Typically, anodization is performed at 40 V in a mixture of 90 vol% ethylene glycol (EG), 10 vol% distilled water, and 0.5 wt% NH₄F as the electrolyte for 1 h. The Ti foil functioned as the anode while the high-density graphite functioned as the cathode.

Subsequently, Cu-sensitized TNT was prepared by using a SILAR method customized from the method reported by Wang and co-researchers [3]. The process began by first dipping the TNT substrates into a Cu(Ac)₂.H₂O solution of selected concentration for a defined duration. This was followed by rinsing with distilled water for 30 s before these substrates were dipped into known concentrations of NaBH₄. The process was completed by a final rinse with distilled water. This was considered as one cycle and it was repeated for a defined number of cycles and period. The illustration for our customized SILAR cycle is shown in Fig. 1. The NaBH₄ solution was prepared fresh in 10 mM NaOH solution (pH 12) to avoid the decomposition of the reagent in water [27]. After the selected number of SILAR cycles has been reached, the electrode was kept in a desiccators prior to further characterization.

To examine the effect of different Cu(Ac)₂.H₂O concentrations, Cu(Ac)₂ and NaBH₄ solutions were varied at 10, 20, 40 and 80 mM. The dipping time was fixed for 10 min and repeated for three SILAR cycles. The resulting electrodes were labeled as CuTNT/10 mM, CuTNT/20 mM, CuTNT/40 mM and CuTNT/80 mM, respectively. The effect of SILAR cycle was investigated by varying the number of cycles at 2, 3, 5, and 7 cycles, and the resulting samples were labeled as CuTNT/2cyc, CuTNT/3cyc,

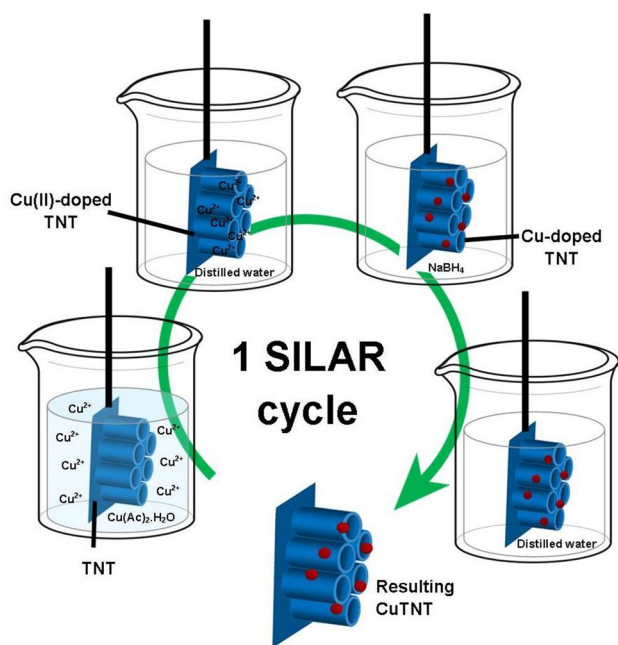


Fig. 1 Process flow of the synthesis of CuTNT via customized SILAR method

CuTNT/5cyc and CuTNT/7cyc, respectively. Finally, to determine the effect of immersion time, the time variation was fixed at 5, 10, 20 and 40 min, and the samples were labeled as CuTNT/5 min, CuTNT/10 min, CuTNT/20 min, and CuTNT/40 min, respectively.

All samples were characterized using a Field Emission Electron Microscope (FESEM) (Carl Zeiss SUPRA 40VP) and an Energy Dispersive X-ray (EDX) (Carl Zeiss SUPRA 40VP). Meanwhile, the X-Ray Diffraction (XRD) (X'Pert Pro-MPD, PANalytical) system was operated at 40 kV and 30 mA, with a scanning range of $2\theta = 10\text{--}90^\circ$ using $\text{Cu K}\alpha$ ($\lambda = 1.504 \text{ \AA}$). X-ray Photoelectron Spectrophotometer (ULVAC-PHI Quantera II) using an $\text{Al-K}\alpha$ (1486.6 eV) radiation source was utilized for XPS signal acquisition. The X-ray was set at 25 W and 15 kV to produce beam size of 100 μm . A survey scan was collected over the range of 0–1200 eV. Narrow scans for Ti 2p, Cu 2p and O1s and a high-resolution spectrum for the Cu $2p_{3/2}$ peak were also obtained. The take-off angle of the photoelectron was set at 45° . An Ultraviolet–Visible Diffuse Reflectance Spectrophotometer (UV-Vis-NIR, Model UV 3600, Shimadzu Corporation, Kyoto, Japan) was also utilized, with a wavelength range of 200–800 nm, and BaSO_4 as the reflectance standard.

For the photoelectrochemical test, a three-electrode cell, equipped with a flat quartz window that was connected to a potentiostat (AUTOLAB), was used to analyze the photoelectrochemical efficiency. The cell consisted of the CuTNTs as the working electrode, a Pt counter electrode,

and an Ag/AgCl reference electrode in 0.5 M NaOH electrolyte. The photoelectrochemical performance was evaluated under sweep potential from +1 V to –1 V with concurrent chopped irradiation from a 300 W halogen lamp (as the visible light supplier) through the quartz window. Besides that, the photocurrent-time analysis was also conducted. As the light was intermittently chopped at a constant frequency, both the ‘dark’ and light-induced photoresponse of the TNT and the CuTNT were assessed in a single experiment.

3 Results and discussion

3.1 Preparation and characterization of titania nanotubes and copper-doped titania nanotubes

3.1.1 Effect of varying the concentration of copper(II) acetate monohydrate solution

Figure 2 shows the growth evolution of Cu-loaded TNTs, which were prepared in various concentrations of copper (II) acetate monohydrate (Fig. 2c–f), with fixed 3 SILAR cycles and 10 min immersion time. Well-aligned and ordered TNT was formed from smooth Ti foil upon anodization as shown in Fig. 2a. The nanotubes were smooth (Fig. 2b) with exposed tops and closed bottoms (inset of Fig. 2a) with outer diameters that ranged between 107 and 143 nm, an inner diameter that ranged between 78 and 104 nm and an average wall thickness of 16.4 ± 2.8 nm. The inset of Fig. 2a shows that the obtained nanotube length was approximately 2.2 μm .

Upon deposition of Cu via SILAR process, small spherical substances were observed to be deposited on top of the TNT, presumably Cu. As low as 10 mM $\text{Cu}(\text{Ac})_2$, Cu particles having 38–66 nm diameter range were successfully deposited on the top mouth of CuTNT/10 mM (Fig. 2c). In CuTNT/20 mM and CuTNT/40 mM (Fig. 2d–e), Cu particles were deposited both into and onto the top surfaces of the TNTs with a diameter range of 36–69 nm and 34–104 nm, with some Cu deposits, respectively. However, the amount of Cu in CuTNT/40 mM was sufficiently large to result in a generous Cu coverage on the TNTs, with bigger particle diameter range and greater clumping. Clumping of the nanotubes and almost a full coverage of Cu were obtained for the CuTNT/80 mM sample. The Cu particles appeared to be less distinctive from each other. The clumping of nanotubes and the deposits of Cu that almost covered the entire TNT may consequently inhibit light absorption by the internal surface area of the TNT—this is undesirable in a photocatalytic application.

The crystal structure of all samples was analyzed using XRD and their spectra are shown in Fig. 3. The pure TNT showed Ti peaks (JCPDS 44-1294) at $2\theta = 35.0^\circ$, 38.45° ,

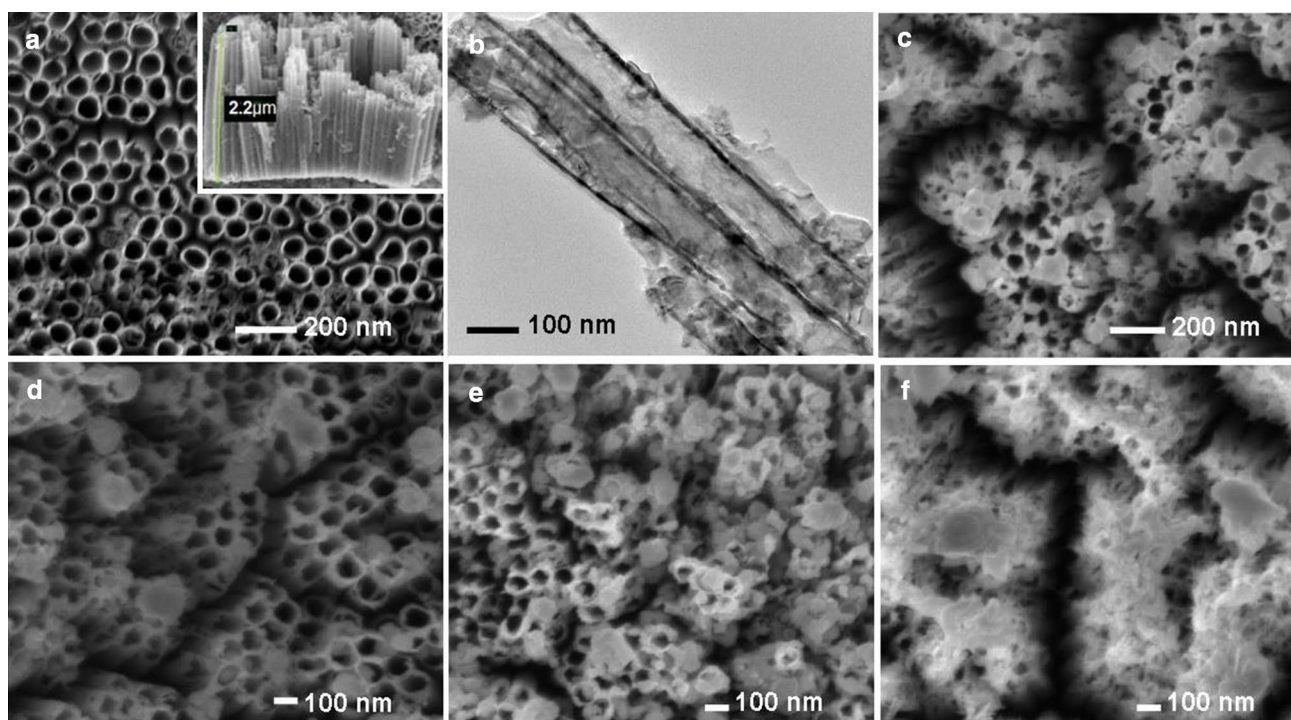


Fig. 2 FESEM micrographs of: **a** pure TNT and its **b** TEM image; FESEM micrographs of **c** CuTNT/10 mM, **d** CuTNT/20 mM, **e** CuTNT/40 mM and **f** CuTNT/80 mM. Inset figure in (a) is the cross-sectional image of pure TNT obtained via FESEM

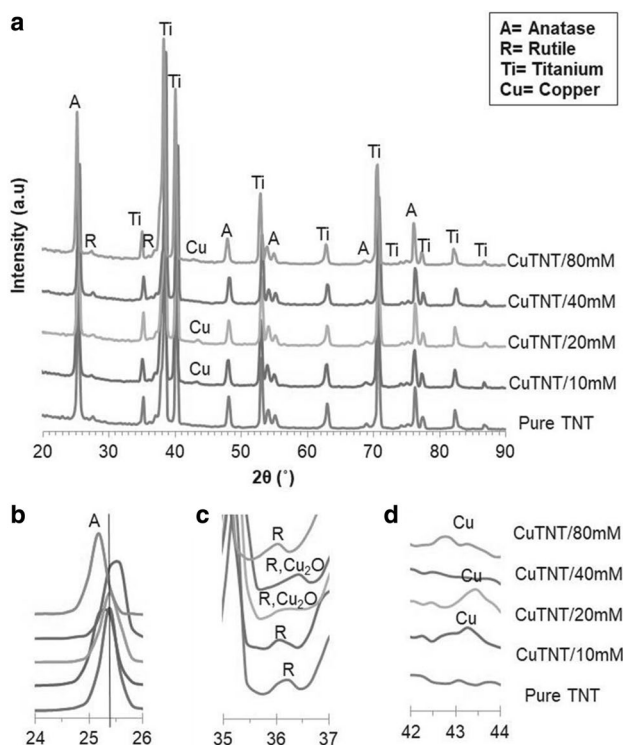


Fig. 3 **a** XRD spectra for pure TNT and CuTNTs prepared from various concentrations; zoom in view at **b** $2\theta = 24\text{--}26^\circ$, **c** $2\theta = 35\text{--}37^\circ$ and **d** $2\theta = 42\text{--}44^\circ$

40.1° , 52.9° , 62.9° , 70.6° , 74.0° , 76.2° , 77.2° , 82.3° , and 86.7° , which corresponded to the (100), (002), (101), (102), (110), (103), (200), (112), (201), (004), and (202) planes, respectively. The pristine TNT has a mixture of anatase and rutile crystalline phases, which improved its crystallinity upon calcination. The anatase phase (JCPDS 21-1272) can be seen as a prominent peak at $2\theta = 25.4^\circ$, corresponding to the (101) plane, and at $2\theta = 37.9^\circ$ (which overlapped the Ti peak). Other anatase peaks include at 48.1° , 53.7° , 55.1° , 68.6° , and 75.0° that corresponded to the (200), (105), (211), (116), and (215) planes, respectively. Minor rutile peaks (JCPDS 21-1276) were detected at $2\theta = 27.4^\circ$ and 36.0° that corresponded to the (110) and (101) planes, respectively.

Cu metal peak (JCPDS 4-0836) at $2\theta = 43.3^\circ$ that corresponded to (111) was observed in the XRD pattern for CuTNT/10 mM, CuTNT/20 mM, and CuTNT/80 mM (Fig. 3a, c). Cu_2O peak (JCPDS 5-0667) could also be detected in certain samples: at $2\theta = 36.4^\circ$ which corresponds to (111) crystalline plane in CuTNT/20 mM and CuTNT/40 mM, which overlapped with rutile TiO_2 of $2\theta = 36.0^\circ$ (refer Fig. 3c). These suggested the successful loading of Cu species in every sample and that the reduction of $\text{Cu}(\text{Ac})_2 \cdot \text{H}_2\text{O}$ in NaBH_4 has possibly resulted in the mixture of Cu species deposited on the CuTNTs. These suggested the successful loading of Cu species into the samples and that the reduction of $\text{Cu}(\text{Ac})_2 \cdot \text{H}_2\text{O}$ in NaBH_4 has possibly resulted in the mixture of Cu species deposited on

the CuTNTs. Shifting of anatase TiO_2 peak at $2\theta = 25.4^\circ$ in CuTNT/10 mM, CuTNT/40 mM and CuTNT/80 mM (Fig. 3b) indicated probable incorporation of Cu species into the TiO_2 crystal lattice.

3.1.2 Effect of varying SILAR cycles

The effect of different SILAR cycles on the formation of CuTNTs was examined at 20 mM of $\text{Cu}(\text{Ac})_2 \cdot \text{H}_2\text{O}$ for 10 min. The morphological changes observed via FESEM are shown in Fig. 4a–d. The CuTNT/2cyc (Fig. 4a) showed a small amount of irregular-shaped Cu particles and also some clumpings deposited on the top of the TNTs. In CuTNT/3cyc (Fig. 4b), Cu particles were observed to be loaded, both into and onto the top of the TNTs with more defined shape and inner and outer diameters as mentioned in Sect. 3.1.1. Increasing the SILAR cycles to 5 for CuTNT/5cyc (Fig. 4c) and 7 for CuTNT/7cyc (Fig. 4d) had significantly increased the number of Cu particles deposited onto the TNTs, with particle diameters that ranged between 56 and 119 nm, and 55 and 134 nm, respectively. However, greater agglomeration as well as noticeably stacking Cu particles, could also be observed. This may be due to the repeated dipping with increasing SILAR cycles that resulted in more Cu particles stacking onto each other by force.

The increasing amount of Cu deposited in FESEM analysis could be supported by the EDX elemental analysis as

Table 2 EDX elemental composition data of CuTNTs of various SILAR cycles

Samples	Weight percentage of elements (wt.%)			
	Ti	O	Cu	C
Blank TNT	58.13	41.12	Not detected	0.75
CuTNT/2cyc	49.32	33.67	16.14	0.87
CuTNT/3cyc	46.77	32.19	20.22	0.82
CuTNT/5cyc	31.92	20.07	47.22	0.78
CuTNT/7cyc	29.90	19.28	49.92	0.91

shown in Table 2. It seems that, upon increasing the SILAR cycles, the proportion of Ti and O were greatly reduced while the proportion of Cu increased. This proved the high coverage of Cu on the TNT surface. The stacking layers of Cu particles with high coverage on the TNTs may be inappropriate in applications involving photogeneration of electrons since this might hinder penetration of light, which can contribute to low photoconversion efficiency.

3.1.3 Effect of varying the immersion time

Figure 5 shows the morphological changes of CuTNTs that were prepared at various immersion times and three SILAR cycles. For CuTNT/5 min, CuTNT/10 min, and CuTNT/20 min (Fig. 5a–c), Cu particles were observed to

Fig. 4 FESEM micrographs of CuTNTs at varied SILAR cycles: **a** CuTNTs/2cyc, **b** CuTNTs/3cyc, **c** CuTNTs/5cyc and **d** CuTNTs/7cyc

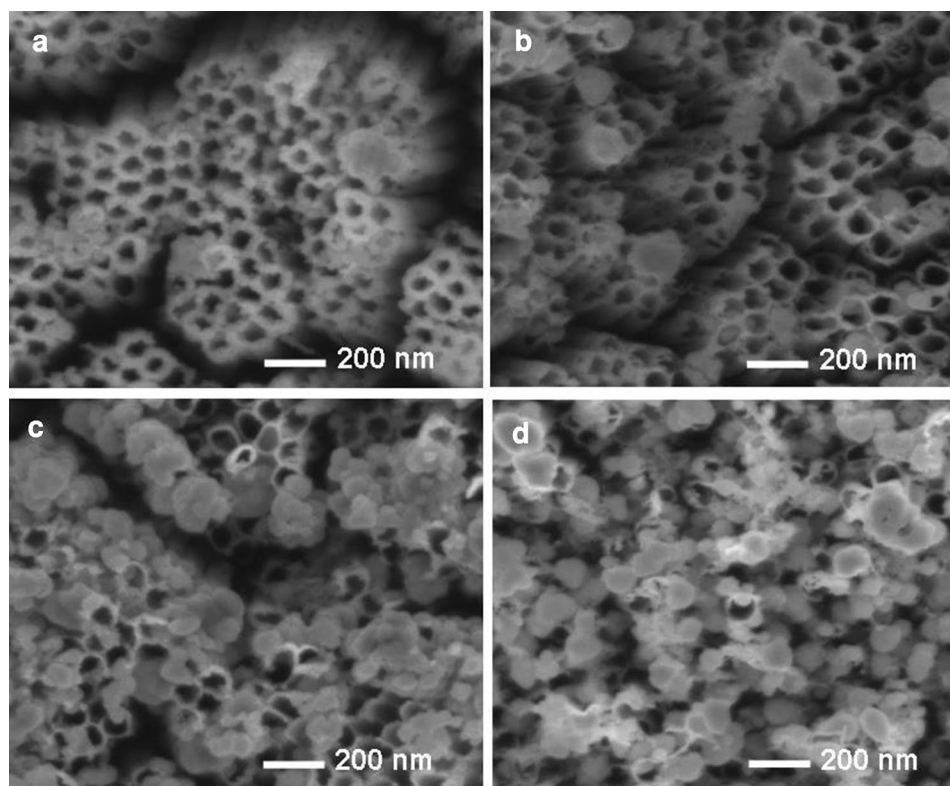
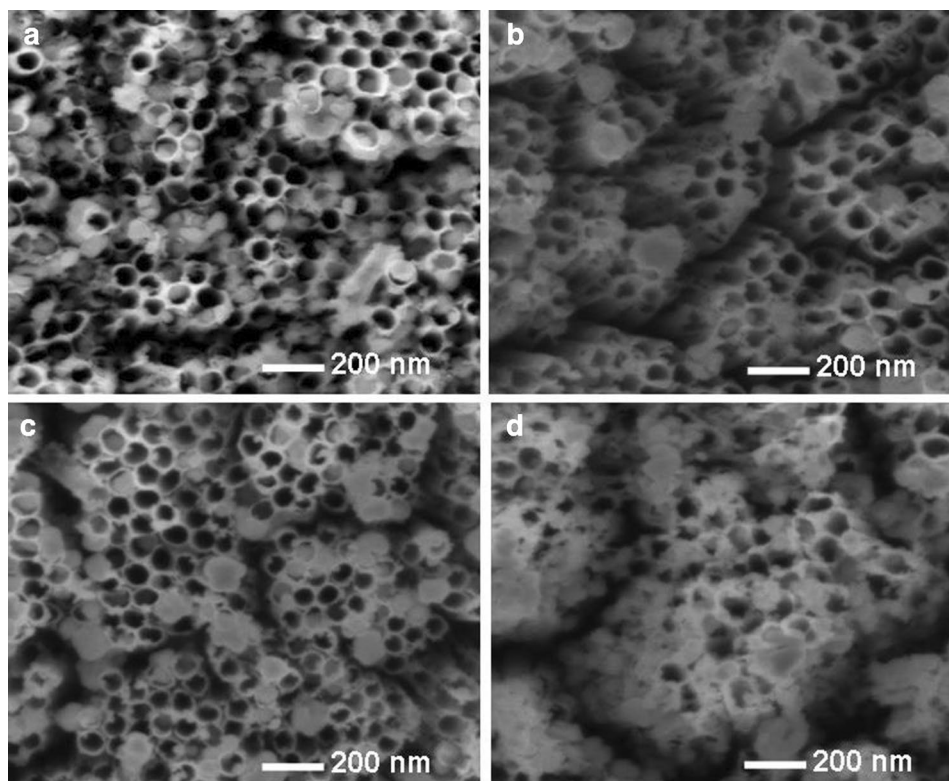


Fig. 5 FESEM micrographs of CuTNTs of varied immersion times: **a** CuTNTs/5 min, **b** CuTNTs/10 min, **c** CuTNTs/20 min and **d** CuTNTs/40 min



be deposited both on the inside and outside of the TNTs. The particles were uniformly distributed, with less agglomeration compared to the CuTNT samples obtained from different SILAR cycles (Fig. 4a–d).

Cu clumps were not observed in the CuTNT/5 min, which could be due to the short dipping time. Nonetheless, defined Cu particles were detected with a diameter range of 21–71 nm in this sample. The particle diameter range for CuTNT/10 min (Fig. 5b) was as stated in Sect. 3.1.1, but with minor Cu deposits. As for CuTNT/20 min (Fig. 5c), the Cu particles have a diameter range of 34–83 nm, with bigger Cu deposits compared to that of the CuTNT/10 min. Thus, lengthening the dipping duration appeared to have increased the amount and the size of Cu particles deposited. This might be due to the prolonged dipping time that allowed more Cu^{2+} ions from $\text{Cu}(\text{Ac})_2$ to be reduced in NaBH_4 .

Overall, lengthening the immersion times instead of increasing the SILAR cycles seems to have resulted in the deposition of Cu particles onto the TNT in a moderate and homogeneous manner (refer to Fig. 6c). Furthermore, the Ti and O proportions in CuTNTs of increasing immersion times seem to be declining moderately as the proportion of Cu increased, as compared to CuTNTs of increasing SILAR cycles (refer to Table 2).

Nevertheless, 40 min of dipping time to fabricate CuTNT/40 min, has resulted in a large network of Cu particles that had almost fully covered the TNT surfaces in CuTNT/40 min (refer Fig. 5d), compared to other CuTNT

samples such as CuTNT/5 min (Fig. 5a), CuTNT/10 min (Fig. 5b) and CuTNT/20 min (Fig. 5c) in which the Cu particles appeared to be in a considerable amount, less distinctive, and formed fewer blockage deposits onto the top of TNT. The high coverage of Cu with less potential of light penetration such in CuTNT/40 min would be detrimental to PEC application. Instead, homogeneity is an important criterion to be considered due to maximized contact between Cu and TiO_2 which in return, enhanced the synergetic effect between these two chemical species.

Table 3 shows the EDX elemental composition data of Ti, O, Cu and C species in blank TNT and all CuTNTs of various immersion times. The detection of Ti and O in all samples based on the EDX elemental composition analysis data confirmed the formation of TiO_2 . C was also detected, which may be due to the decomposition of ethylene glycol during the anodization process. However, the wt% of C was so marginal that it could be considered as negligible. The detection of Cu species further proves the successful fabrication of CuTNTs.

Therefore, in order to investigate the Cu species present, an X-Ray Photoelectron Spectroscopy (XPS) analysis was conducted. Figure 7 shows the XPS spectrum of the resulting sample. The binding energy for Ti $2p_{3/2}$ and Ti $2p_{1/2}$ (refer Fig. 7a) were located at 458.5 eV and 464.3 eV respectively, suggesting that the resulting CuTNT possessed Ti of predominant oxidation state Ti^{4+} . The detection of Ti peaks as Ti^{4+} or as TiO_2 was agreeable with other findings

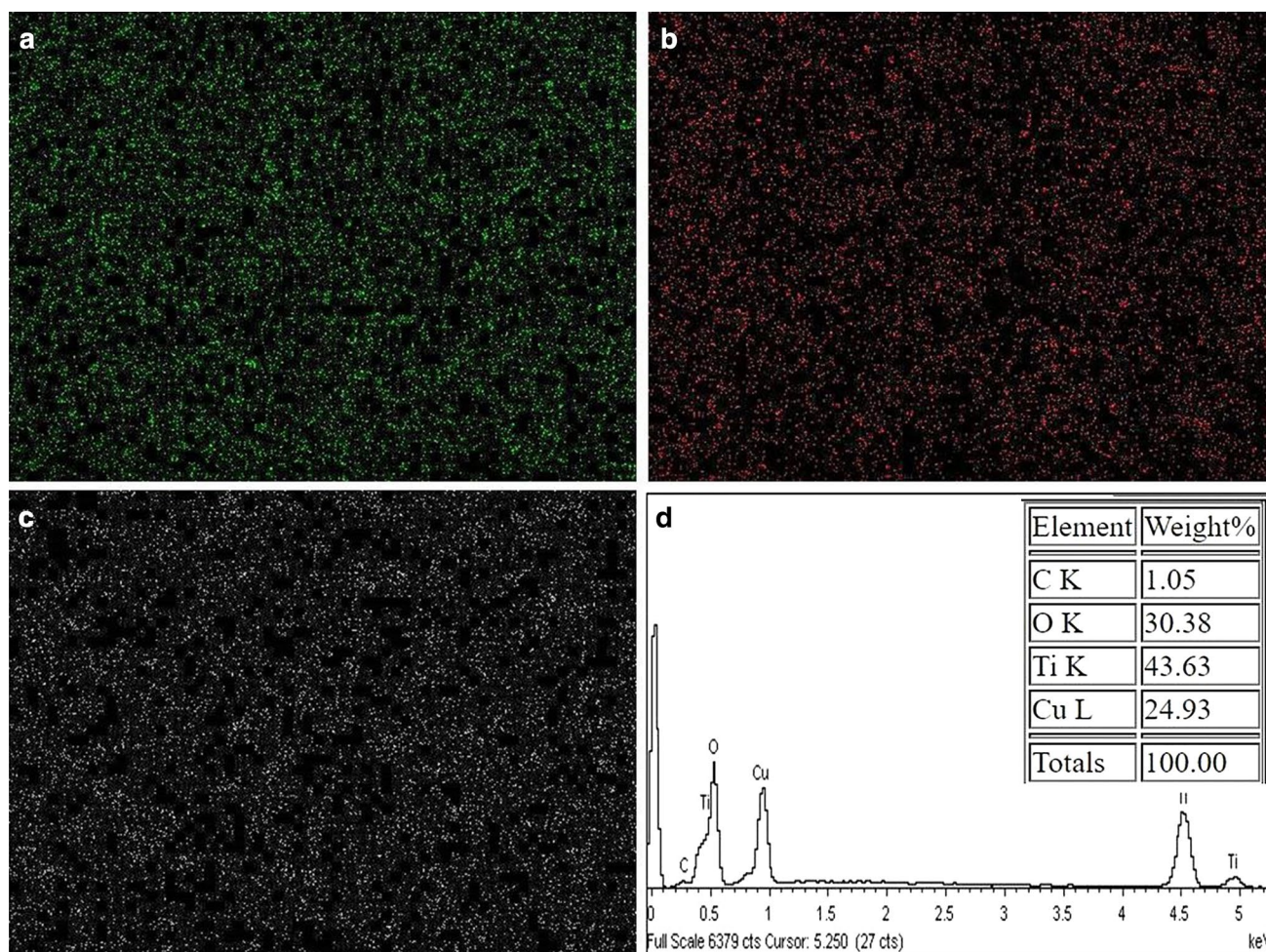


Fig. 6 EDX elemental mapping of **a** Ti, **b** O and **c** Cu; and **d** EDX spectrum of CuTNT/20 min

Table 3 EDX elemental composition data of CuTNTs of various immersion times

Samples	Weight percentage of elements (wt.%)			
	Ti	O	Cu	C
Blank TNT	58.13	41.12	Not detected	0.75
CuTNT/5 min	46.23	32.38	20.74	0.65
CuTNT/10 min	46.77	32.19	20.22	0.82
CuTNT/20 min	43.63	30.38	24.93	0.78
CuTNT/40 min	39.94	26.35	32.75	0.97

[25, 28, 29]. Figure 7b shows Cu $2p_{3/2}$ and Cu $2p_{1/2}$ peaks at 932.5 and 952.7 eV, close to the binding energies of Cu metal as reported by [17]. However, the binding energy values were comparable to that of Cu_2O [21] which suggested the possible existence of both Cu metal and Cu_2O as proven in XRD analysis (Fig. 3). On the other hand, the shake-up lines observed at around 945.0 and 962.8 eV could be attributed by the partially filled Cu^{2+} 3d orbitals ($3d^9$) [30].

Hence, deconvolution was made on Cu $2p_{3/2}$ peak to confirm the chemical species of Cu present and was shown in Fig. 7c. The atomic concentration of Cu present in possible chemical species was as tabulated in Table 4.

From Fig. 7c, a strong peak at 932.5 eV was observed, indicating a high concentration of the mixture of Cu/ Cu_2O on the sample surface. This can be proven by the high amount of Cu/ Cu_2O detected as shown in Table 4. Cu^{2+} chemical state was also present in the form of CuO which was exhibited at higher binding energy 933.9 eV and also at 935.0 eV in the form of $\text{Cu}(\text{OH})_2$ as claimed by [18], with the comparable amount. This suggested that the Cu species deposited on the CuTNT sample was consisting of the mixture of Cu metal, Cu_2O , CuO and $\text{Cu}(\text{OH})_2$, upon the chemical reduction of Cu^{2+} ions adsorbed onto the TNT, in NaBH_4 reducing reagent.

The chemical species of Cu present could also be supported upon deconvolution of O 1s peak (refer Fig. 7d) which indicates the O1s in the CuO lattice at 529.6 eV and the O1s of the $-\text{OH}$ group at 531.5 eV as reported by

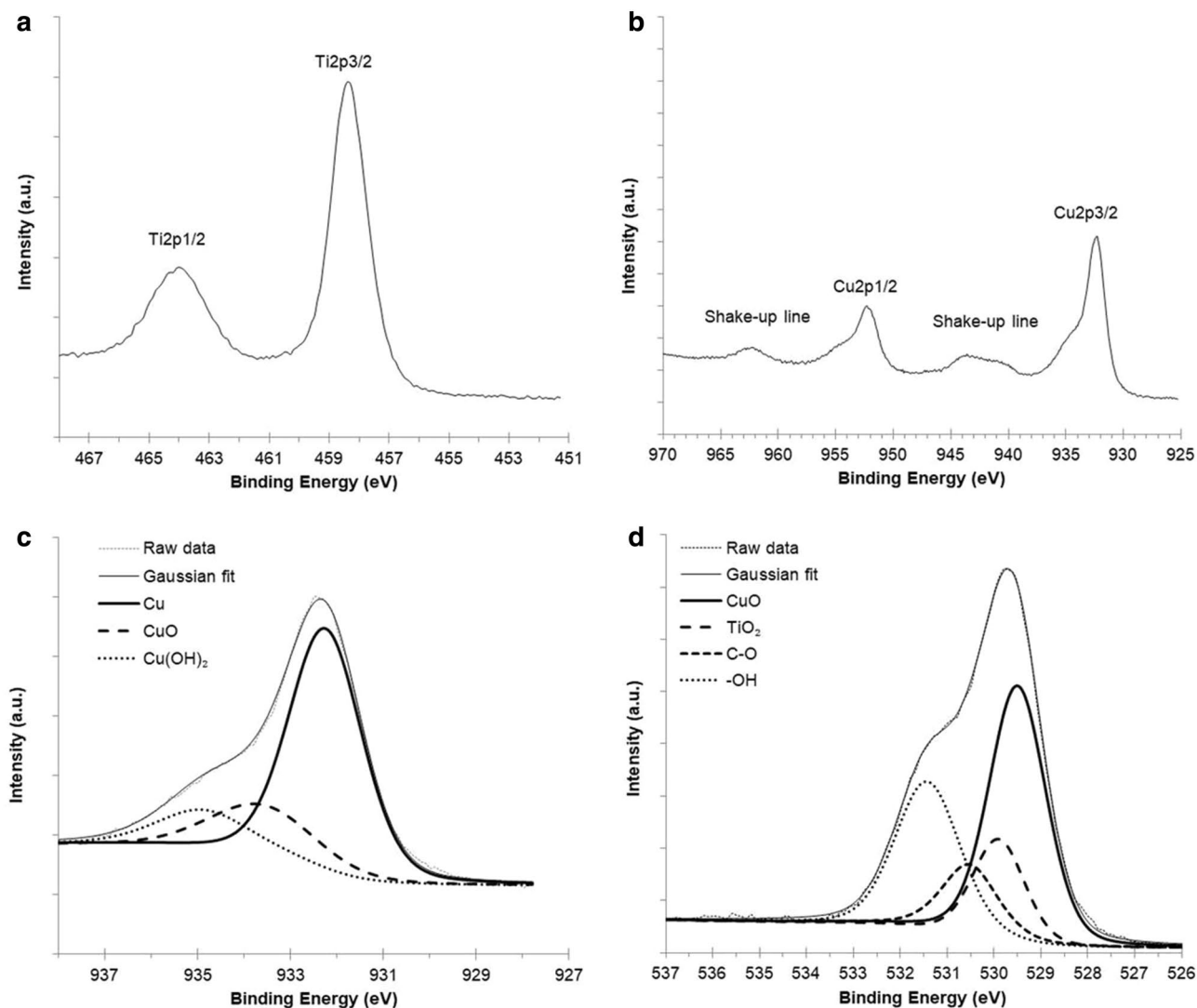


Fig. 7 XPS narrow scan spectrum of **a** Ti 2p and **b** Cu 2p; **c** high resolution narrow scan with deconvolution of Cu 2p_{3/2} from 938 to 927 eV and **d** O 1 s

Table 4 Atomic concentration of Cu 2p and O 1 s in respective chemical species present in CuTNT/20 min

Chemical states	Chemical species	Chemical composition (at.%)
Cu 2p	Cu/Cu ₂ O	65.58
	CuO	19.74
	Cu(OH) ₂	14.68
O 1 s	TiO ₂	15.35
	CuO	43.76
	C-O	12.81
	-OH	28.08

Akhavan and co-researchers [18]. The O 1 s of –OH group detected was consistent with the amount of Cu detected in Cu(OH)₂ (refer Table 4) and hence supported the observation that Cu(OH)₂ was present.

3.2 Photoelectrochemical (PEC) performance

To further elucidate the advantages of depositing Cu onto TNT, the photoresponses of blank Ti, pure TNT and the obtained CuTNT samples were examined via PEC test. Several on–off illumination cycles were conducted where both ‘dark’ and light-induced photoresponses were assessed in a single experiment, as shown in Fig. 8. Figure 8a illustrates the enhanced photocurrent of TNT compared to blank Ti. It can be seen that the blank Ti sample exhibited a negligible photocurrent and very high dark

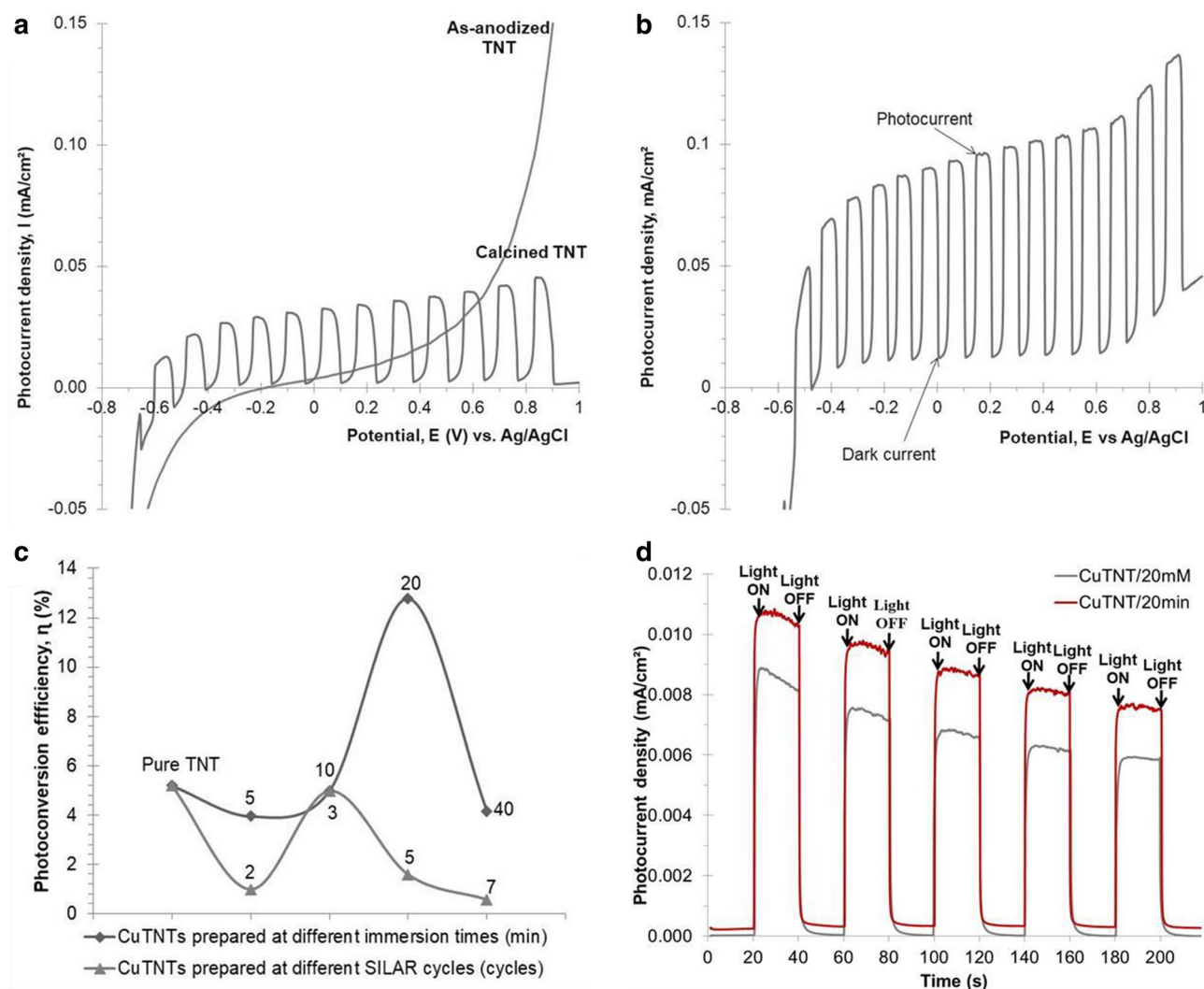


Fig. 8 Photoresponses of **a** as-anodized TNT and calcined TNT and **b** CuTNTs/20 min with optimum 3 SILAR cycles and 20 mM concentration; **c** the trend of the calculated photoconversion efficiency per-

current at positive potentials. On the contrary, pure TNT exhibited enhanced photocurrent and negligible dark current across the implied potentials. Such enhancement in photoresponse is supported by several factors: (i) the high surface area of the nanotubular structure of the TNTs that enhances the charge transport [1], and (ii) the crystallinity of the TNTs, which directly channels the photogenerated electrons towards the Ti substrate [31], specifically anatase TNT that suppresses the recombination of charged carriers better than rutile TNT [1].

Figure 8b shows higher enhancement in photoresponse upon the deposition of Cu in CuTNT/20 min as the photocurrent density was doubled. This could be attributed to the presence of Cu species that served as an electron trap center which helps reduce electron–hole recombination [19], thus increases the lifetime of the electrons.

formance of CuTNTs of various SILAR cycles and immersion time; and **d** the $I-t$ curves of CuTNT/20 mM and CuTNT/20 min at -0.2 V

The photoconversion efficiency (η) for all samples was measured at -0.3 V potential versus Ag/AgCl electrode. Equation 1 as stated by [32] was used, where I_0 refers to photocurrent density (A/m^2), V_{bias} refers to applied potential, and J_{light} refers to light irradiance (W/m^2). The trend of the calculated η values is shown in Fig. 8c.

$$\eta = \frac{I_0(1 \cdot 23 - V_{bias})}{J_{light}} \quad (1)$$

The deposition of Cu species onto TNT in various SILAR cycles has led to a decrease in the photoconversion efficiency in most of the CuTNT samples, as illustrated by Fig. 8c. This might be due to big-sized Cu particles, or by the deposits of Cu particles that decrease the penetration of light into the nanotubes for photo-energy conversion.

The declining PEC performance can be seen from the η values; from 2.24% in pure TNT to 0.31% in CuTNT/2cyc, 0.57% in CuTNT/5cyc, and 0.62% in CuTNT/7cyc. A sudden increase in η value at 2.45% in CuTNT/3cyc suggested that the optimum SILAR cycle to synthesize CuTNT would be three cycles.

The general trend of PEC performance, however, was better in CuTNTs of various immersion times compared to those of various SILAR cycles. This is shown by the higher values of η at 1.76% in CuTNT/5 min, 2.45% in CuTNT/10 min, 6.21% in CuTNT/20 min, and 2.49% in CuTNT/40 min. This observation could be attributed to the uniform distribution of Cu particles into and onto the TNTs of various immersion times, which allowed light to channel through the TNTs more efficiently. On the other hand, the severe clumping and the layer-like of Cu that covered the CuTNTs of various SILAR cycles could have limited the penetration of light.

Among these samples, CuTNT/20 min, with the optimum 20 mM and 3 SILAR cycles, showed 2.7 times better PEC performance compared to that of pure TNT. Besides having enhanced photo-light conversion efficiency performance, CuTNT/20 min also showed an overall good photocurrent reproducibility over time as observed in Fig. 8d, similar to CuTNT/20 mM. This suggests that the CuTNTs obtained exhibit good electrode stability. This can be further supported by FESEM images in Fig. 9a, b which shows no obvious change of morphology of Cu after PEC test was conducted.

The enhanced performance of CuTNT/20 min could be due to the balanced distribution of Cu species in the TNTs, with fewer blockages on the TNTs, as shown by the FESEM images. These are significant factors that could increase the contact between Cu species and TiO_2 , inside and outside of the TNT, which can lead to more effective light exposure as well as a balanced electron pathway between these two chemical species. Thus, the positive impacts induced by Cu species towards the TNTs were not merely based on Cu being the electron trap center, but its optimum particle size, concentration, and uniform

distribution had also contributed towards maximizing the synergetic effect between Cu species and TiO_2 .

3.3 Ultraviolet–Visible diffuse reflectance spectroscopy (UV-DRS) analysis

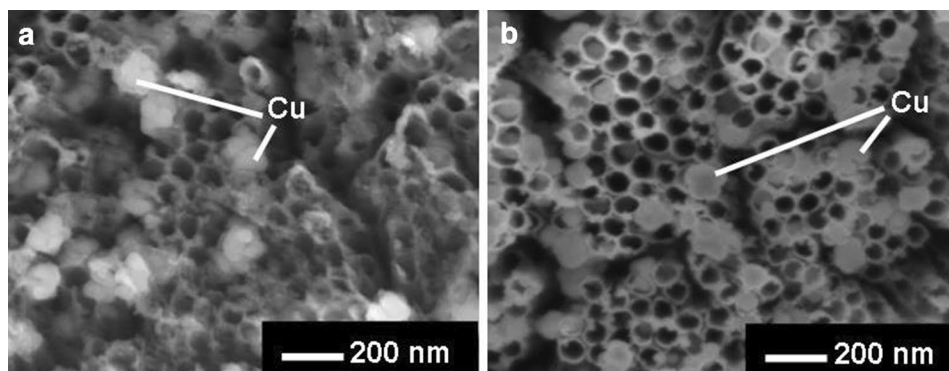
UV-DRS analysis was performed to establish the synergetic effect between Cu species and TiO_2 , as shown in Fig. 10. The band gap energy (E_g) was calculated using Eq. 2 as according to Yang and co-researchers [33]. The wavelengths (λ) absorbed by the samples were obtained by extrapolating the sudden drop of absorbance or absorption edge from 380 nm, as shown in Fig. 10a.

$$E_g = \frac{1240}{\lambda} \quad (2)$$

The bare TNT, as shown in Fig. 10a exhibited a strong UV light absorbance at $\lambda < 380$ nm. The UV light absorption can be attributed to the intrinsic band gap absorption of TiO_2 [34]. Upon the deposition of Cu, the band gap absorption edge shifted to approximately 420 nm, as shown in Fig. 10a, which lowered the band gap from 3.26 eV (pure TNT) to 2.95 eV. However, the higher content of Cu in CuTNT/7cyc, and CuTNT/40 min had decreased the absorption of UV light, and increased the absorption of visible light, as shown in Fig. 10b. The high visible light absorbance was due to the domination of Cu on the TNT surface since the surface Plasmon resonance of Cu is at a wavelength range of 580 to 600 nm [35]. These results further prove the decreased penetration of light through the TNTs, as shown by the FESEM morphological analysis. Consequently, the decrement of UV light absorbance in UV-DRS, and also the lower PEC performance were observed. On the other hand, CuTNT/20 min which showed the highest performance improvement, exhibited both strong UV and visible light absorption capabilities, with an increased redshift, as shown in Fig. 10a, which lowered the band gap to 2.75 eV.

Nevertheless, in explaining the relationship between the band gap narrowing effect towards the PEC performance of CuTNT might require an explanation from the Cu species

Fig. 9 FESEM images of **a** CuTNT/20 min before PEC and **b** CuTNT/20 min after PEC



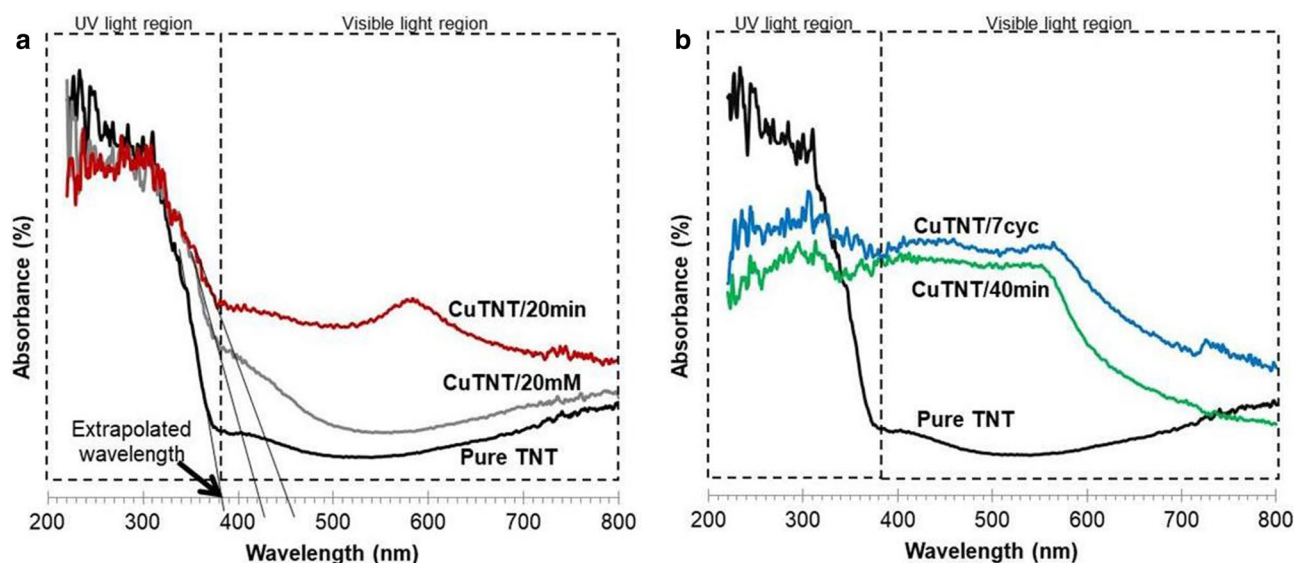


Fig. 10 UV-DRS spectra of **a** pure TNT, CuTNT/20 mM and CuTNT/20 min; and **b** pure TNT, CuTNT/7cyc and CuTNT/40 min

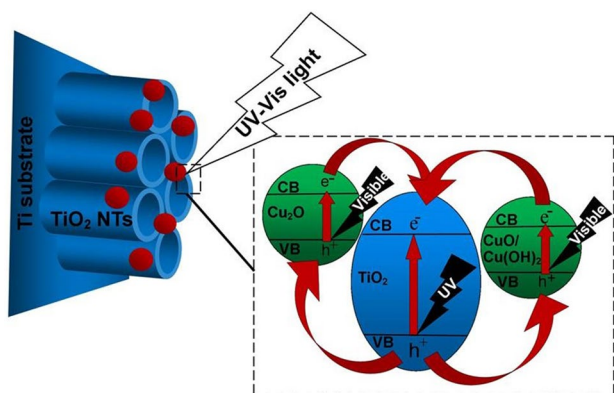


Fig. 11 Possible mechanisms that are involved during the illumination of light

itself. It is noted that in this study, four Cu species were deposited onto the CuTNT samples: Cu metal, Cu_2O , CuO and $\text{Cu}(\text{OH})_2$ semiconductors. It is understood that in a metal such as Cu, the valence band (VB) and the conduction band (CV) is expected to overlap and hence might not contributing towards the electron trap effect on TNT. Cu_2O , CuO and $\text{Cu}(\text{OH})_2$ on the other hand, are semiconducting materials with distinguished VB and CB; and the difference between these two chemical species' transition bands with that of TNT aids in the electron trap effect which functions to reduce the electron–hole recombination rate of TNT. The possible mechanisms could be illustrated via Fig. 11.

First, electrons were excited from the VB of TiO_2 and Cu species ($\text{Cu}_2\text{O}/\text{CuO}/\text{Cu}(\text{OH})_2$) to their CB due to their absorption in the UV light region and the visible light

region, respectively. The strong UV light absorption in CuTNT/20 min (Fig. 10a) was due to the fewer blockages, which enabled light to penetrate and excite TiO_2 electrons. On the other hand, the visible light absorption was due to the visible-light reactive Cu species on the surface of the TNTs. Such broad utilization of the light spectrum will eventually lead to an effective photocatalytic activity [35]. Second, since the VB of TiO_2 is more positive than that of Cu_2O and CuO, photogenerated electrons in the conduction band of Cu species would be transferred to TiO_2 . Similarly, the photogenerated holes in the valence band of TiO_2 would be transferred to Cu species. Hence, a wide electron–hole separation was achieved where the photogenerated electrons and holes were separated into the CB of TiO_2 and the VB of Cu species, respectively. This reaction is able to reduce the recombination of the electron–hole pairs, which was also observed by Sun and co-researchers [36] hence explains the electron-trap center induced by the Cu species, which had enhanced the photocatalytic efficiency.

4 Conclusion

Well-ordered crystalline TNT with a mixture of anatase phase (major) and rutile phase (minor) was obtained upon anodization. Cu-loaded TNTs were successfully obtained via SILAR method, as proven by FESEM, EDX, and XRD analyses. The amount of Cu deposited onto the TNTs had increased with increasing Cu^{2+} concentration, SILAR cycles, and immersion time. The Cu deposited, as investigated via XPS analysis, was consisting of major $\text{Cu}/\text{Cu}_2\text{O}$ and a comparable amount of CuO and $\text{Cu}(\text{OH})_2$. CuTNT/20 min,

with a fixed 20 mM solution concentration and 3 SILAR cycles, exhibited the best PEC performance with 2.7 times enhancement compared to pure TNT with good electrode stability. UV-DRS analysis has confirmed the synergetic effect induced by Cu, which can be seen by the redshift with CuTNT/20 mM and CuTNT/20 min. This condition led to the reduced band gap, from 3.26 eV in pure TNT to 2.95 eV in CuTNT/20 mM, and 2.75 eV in CuTNT/20 min as well as the broad utilization of light spectrum exhibited by CuTNT/20 min. The enhanced PEC performance of CuTNT, therefore, could be attributed to several factors: the high surface area of the nanotubular structure; the crystallinity of the TNT that contributed towards the enhancement of electron channels towards Ti substrate; the effect of the electron-trap centre introduced by Cu towards the TNTs; the reduced band gap energy; the broader utilization of light spectrum; and the uniformed distribution of Cu species in TiO₂ NT which allowed better light penetration and maximised the synergetic effect between these two chemical species.

Acknowledgements This work was funded by Ministry of Higher Education Malaysia through the FRGS Grant (FRGS/1/2017/STG07/UITM/03/4).

References

1. Y. Zhao, N. Hoivik, K. Wang, *Nano Energ.* **30**, 728–744 (2016)
2. P. Roy, S. Berger, P. Schmuki, *Angew. Chemie.* **50**, 13, 2904–2939 (2011)
3. Q. Wang, R. Jin, M. Zhang, S. Gao, *J. Alloys Compd.* **690**, 139–144 (2017)
4. M.M. Momeni, Y. Ghayeb, *J. Alloys Compd.* **637**, 393–400 (2015)
5. E.A. Al-Arfaj, *Superlattices Microstruct.* **62**, 285–291 (2013)
6. J. Liu, B. Liu, Z. Ni, Y. Deng, C. Zhong, W. Hu, *Electrochim. Acta* **150**, 146–150 (2014)
7. M.M. Momeni, Y. Ghayeb, *J. Appl. Electrochem.* **45**(6), 557–566 (2015)
8. N.F.A. Harun, Y. Mohd, L.Y. Pei, L.Y. Chin, *Int. J. Electrochem. Sci.* **13**, 5041–5053 (2018)
9. M.M. Momeni, Z. Nazari, *Ceram. Int.* **42**, 7, 8691–8697 (2016)
10. J. Xue, Q. Shen, F. Yang, W. Liang, X. Liu, *J. Alloys Compd.* **607**, 163–168 (2014)
11. M.M. Momeni, A.A. Mozafari, *J. Mater. Sci. Mater. Electron.* **27**, 10, 10658–10666 (2016)
12. M.M. Momeni, Y. Ghayeb, Z. Ghonchehi, *J. Solid State Electrochem.* **19**(5), 1359–1366 (2015)
13. P.K. Dubey, R. Kumar, A.C. Pandey, R.S. Tiwari, O.N. Srivastava, *Int. J. Hydrogen Energy* **42**, 8, 4782–4792 (2017)
14. M.M. Momeni, *Appl. Surf. Sci.* **357**, 160–166 (2015)
15. S.S. Tafreshi, A. Roldan, N.Y. Dzade, N.H. De Leeuw, *Surf. Sci.* **622**, 1–8 (2014)
16. M. Khraisheh, L. Wu, A.H. Al-Muhtaseb, M.A. Al-Ghouti, *J. Ind. Eng. Chem.* **28**, 369–376 (2015)
17. S. Zhang, H. Wang, M. Yeung, Y. Fang, H. Yu, F. Peng, *Int. J. Hydrogen Energy* **38**, 18, 7241–7245 (2013)
18. O. Akhavan, R. Azimirad, S. Safa, E. Hasani, *J. Mater. Chem.* **21**, 26, 9634 (2011)
19. R.A. Doong, C.W. Tsai, *J. Taiwan Inst. Chem. Eng.* **57**, 69–76 (2015)
20. T. Han, D. Zhou, H. Wang, *Powder Technol.* **301**, 959–965 (2016)
21. Y. Liu, H. Zhou, J. Li, H. Chen, D. Li, B. Zhou, W. Cai, *Nano-Micro Lett.* **2**(4), 277–284 (2010)
22. S. Zhang, S. Zhang, F. Peng, H. Zhang, H. Liu, H. Zhao, *Electrochem. commun.* **13**, 8, 861–864 (2011)
23. K.G. Stamplecoskie, J.S. Manser, *ACS Appl. Mater. Interfaces* **6**, 20, 17489–17495 (2014)
24. M.M. Momeni, Y. Ghayeb, A.A. Mozafari, *J. Mater. Sci. Mater. Electron.* **27**, 11, 11201–11210 (2016)
25. R.N. Bulakhe, N.M. Shinde, R.D. Thorat, S.S. Nikam, C.D. Lokhande, *Curr. Appl. Phys.* **13**, 8, 1661–1667 (2013)
26. Y.C. Lim, Z. Zainal, W.T. Tan, M.Z. Hussein, *Int. J. Photoenerg.* (2012). <https://doi.org/10.1155/2012/638017>
27. S. Petit, K. David, J.-P. Doumerc, J.-C. Grenier, T. Seguelong, M. Pouchard, *Comptes Rendus de l'Académie Des Sci. Series IIC Chem.* **1**, 8, 517–522 (1998)
28. S.S. Kale, R.S. Mane, H. Chung, M.Y. Yoon, C.D. Lokhande, S.H. Han, *Appl. Surf. Sci.* **253**, 2, 421–424 (2006)
29. C.M. Muiva, K. Maabong, C. Moditswe, *Thin Solid Films* **616**, 48–54 (2016)
30. R. Sahay, J. Sundaramurthy, P. Suresh Kumar, V. Thavasi, S.G. Mhaisalkar, S. Ramakrishna, *J. Solid State Chem.* **186**, 261–267 (2012)
31. L.Y. Chin, Z. Zainal, M.Z. Hussein, T.W. Tee, *J. Nanosci. Nanotechnol.* **11**(6), 4900–4909 (2011)
32. H. Wu, Z. Zhang, *J. Solid State Chem.* **184**(12), 3202–3207 (2011)
33. Y.Y. Yang, L.X. Zhou, Y.Q. Zheng, H.L. Zhu, W.Y. Li, *J. Solid State Chem.* **253**, 211–218 (2017)
34. M.M. Momeni, Y. Ghayeb, S. Gheibee, *Ceram. Int.* **43**(1), 564–570 (2017)
35. F. Parveen, B. Sannakki, M.V. Mandke, H.M. Pathan, *Sol. Energy Mater. Sol. Cells* **144**, 371–382 (2016)
36. H. Sun, B. Dong, G. Su, R. Gao, W. Liu, L. Song, L. Cao, *Appl. Surf. Sci.* **343**, 181–187 (2015)